

# Investigation of Mechanical Strength and Fatigue Crack Growth Behaviour of Hot-Rolled SUP9 Steel for Leaf Spring Suspension Application

M. Badaruddin<sup>1,\*</sup>, A. K. Purga<sup>1</sup>, Sugiyanto<sup>1</sup>, D. Asmi<sup>2</sup>, S. Sumardi<sup>3</sup>, A. L. Indratmoko<sup>3</sup>

\* *mbruddin@eng.unila.ac.id*

<sup>1</sup> Study Program of Magister-Department of Mechanical Engineering, Faculty of Engineering Universitas Lampung

<sup>2</sup> Study Program of Magister-Department of Physics, Faculty of Mathematics and Faculty of Mathematics and Natural Science, Universitas Lampung

<sup>3</sup> Research Unit for Mineral Technology, National Research and Innovation Agency (BRIN), Tanjung Bintang, Lampung Selatan-Indonesia

<sup>4</sup> Polytechnic of Tunas Garuda, Department of Manufactural Engineering, Lampung, Indonesia

**Received: September 2024**

**Revised: December 2024**

**Accepted:**

**Abstract:** The investigation of SUP9 steel under the hot-rolling conditions for applications to leaf spring suspension focused on its tensile and fatigue crack growth (FCG) properties. In order to investigate the tensile properties, tensile specimens were fabricated in the longitudinal-transverse (LT) direction. Furthermore, in order to evaluate fatigue crack growth (FCG) behaviour, compact tensile (CT) specimens with different crack plane orientations in both the LT and transverse-longitudinal (TL) directions were employed. Microstructural and fractographic analyses were conducted using optical microscope (OM) and scanning electron microscopy (SEM). The hot-rolling process reduced the interlamellar spacings of  $Fe_3C$ , enhancing the tensile properties through strain hardening. A high yield-to-ultimate strength ratio ( $\sim 0.623$ ) indicates excellent plastic deformation capability and resistance to fatigue crack growth, making SUP9 steel suitable for the leaf spring suspension system. Furthermore, the exponential crack growth rate constant,  $m$ , was found to be 3.066 in the TL direction and 3.265 in the LT direction, indicating that cracks propagate more rapidly in the LT orientation. Additionally, non-metallic inclusions, such as spherical oxides and MnS precipitates in LT specimens, were observed to facilitate faster crack growth in the transverse direction.

**Keywords:** SUP9 steel, Hot-rolling, Lamellar  $Fe_3C$ , Manganese sulphide, Crack growth rate

## 1. INTRODUCTION

SUP9 steel plate, manufactured through the hot-rolling process, is a highly versatile material widely used for leaf spring suspension components in industrial transportation. It is a popular choice for

suspension systems in heavy-duty vehicles, including trucks, SUVs, buses, railway wagons, and vans [1], owing to its cost-effective production and straightforward maintenance requirements. The suspension system, comprising a leaf spring, is typically assembled using a semi-elliptical laminate model [2]. This system is a vital component of any vehicle, providing support while absorbing and releasing cyclic loading in a controlled manner [3]. To ensure the initial safety design of leaf spring suspension components can effectively support heavy-duty vehicles, SUP9 steel must meet specific mechanical properties, including mechanical strength and resistance to fatigue crack growth.

Cyclic or dynamic load-induced fatigue is a significant issue affecting the components of leaf springs in heavy-duty vehicles [3,4]. Several studies have been conducted to enhance the strength of leaf spring steel by applying quenching-tempering (QT) heat treatments [2,5] and the shot peening technique [6,7]. QT changes the pearlite-ferrite structure to the required tempered martensite structure. In addition, shot peening induces compressive residual stresses throughout the thickness of the component. However, the most severely tempered martensite phase exhibits a limited capacity for plastic deformation, which can result in the brittle fracture of the leaf spring steel. Strain hardening results in a hard martensite microstructure and a weak ferrite phase, thereby increasing high-stress concentration [8-11]. Similar mechanisms in leaf spring steel, shot peened, give rise to the initiation of cracks at the interface between zones of compressive and tensile stress [7]. However, an investigation into the tensile and fatigue crack growth performance of SUP9 steel in hot-rolling conditions, with respect to its pearlitic structural characteristics, has yet to confirm whether such structures exhibit enhanced fatigue crack resistance [12-13]. Pearlitic structures within the steel strengthen its capacity for plastic deformation, thereby facilitating the postponement of crack propagation over more extended fatigue cycles [14,15]. It is important to highlight that the microstructure significantly impacts the fatigue crack growth of leaf spring steel.

In the context of suspension systems in heavy-duty vehicles, it has been observed that the predominant failure of leaf spring components occurs in the LT direction, accompanied by the accumulation of crack initiations in the fatigue crack area. As the number of fatigue cycles increases, these initial cracks gradually expand and converge [16]. Furthermore, microstructural defects, such as non-metallic oxides and sulphides, have been shown to cause rapid cracking, leading to catastrophic failure [17,18].

Therefore, this study aims to investigate the mechanical strength and fatigue crack growth behaviour of hot-rolled SUP9 steel, providing valuable insights for designing and engineering resilient leaf spring suspensions. Additionally, microstructural observations were conducted using an optical microscope (OM). Observations of fracture morphologies of FCG specimens were carried out using scanning electron microscopy (SEM), combined with elemental analysis via EDS, to elucidate the comprehensive FCG behaviour of SUP9 leaf spring steel.

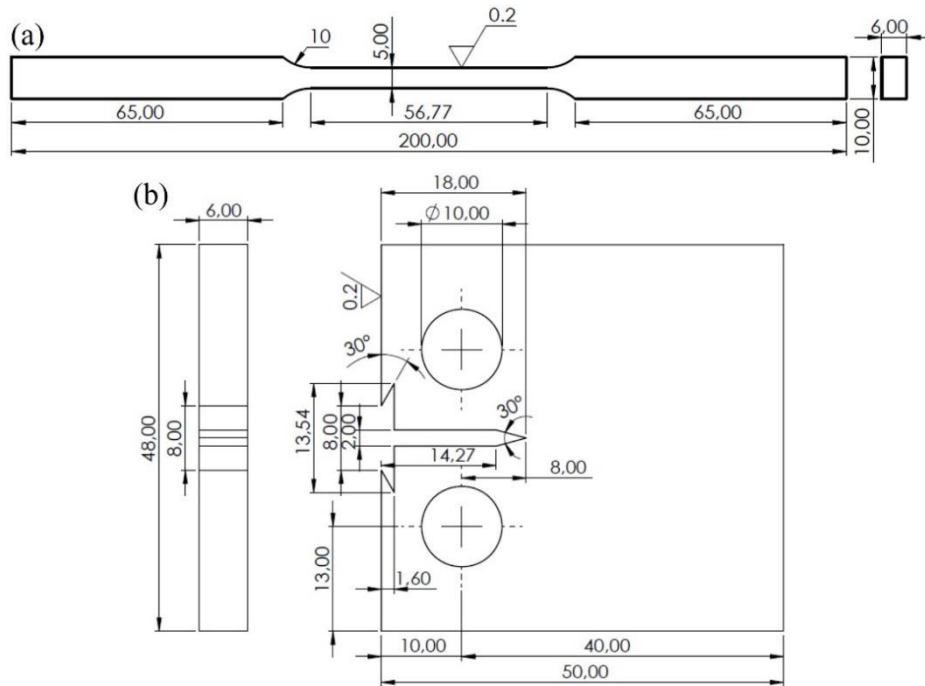


Fig. 1. The geometry of (a) the tensile specimen and (b) the CT specimen (units in mm)

## 2. EXPERIMENTAL PROCEDURE

### 2.1 Material and Specimen Preparation

The dimensions of the original SUP9 steel, delivered in hot-rolled form, were as follows: The material was 6 mm thick, 65 mm wide, and 6000 mm long. A 200 mm length was cut from the flat SUP9 steel. The chemical composition of SUP9 steel is as follows: 0.52%C, 0.15%Si, 0.65%Mn, 0.03%P, 0.045%S, 0.65%Cr, with the remainder being iron (Fe) (wt.%). Tensile testing involved the use of two specimens (designated as Sp\_1 and Sp\_2), which were tested in the longitudinal-transverse direction (LT) in accordance with the ASTM E8 standard [19]. Fatigue crack growth (FCG) testing used four compact tension (CT) specimens, as per the ASTM E647 standard [20]. Two CT specimens were

oriented in the LT direction, and two others in the transverse-longitudinal direction (TL). The shape and dimensions of the tensile and FCG specimens are shown in Figs. 1a and 1b, respectively.

## 2.2 Mechanical Characterisation

The axial tensile and FCG tests were conducted using a computerised servo-hydraulic MTS Landmark 100 kN. An extensometer (MTS 634.25F-24 type) with a 50 mm gauge length was used to measure the length changes in the axial direction. The specimen was pulled at a constant force rate of 0.2 kN/s [19] until it reached its breaking point. A data acquisition system (DAQ), integrated with a MTS FlexTest40 controller, was used to record incremental force and axial length changes. The data were converted from kN per mm<sup>2</sup> and mm per 50 mm gauge length to MPa and mm/mm, respectively, using a Python program to provide the relevant stress and axial strain. Subsequently, a stress-strain curve was constructed to determine yield strength ( $\sigma_{yield}$ ) using the 0.2% offset method, ultimate strength ( $\sigma_{ult}$ ), elastic modulus ( $E$ ), and elongation ( $e$ ). Furthermore, the strain-hardening properties were established according to the ASTM E646 standard, comprising the strain-hardening constant ( $K$ ) and the exponential constant ( $n$ ) [21]. Additionally, the hardness of SUP9 steel was assessed using a Zwick Roell micro-Vickers (EMCO-Test) under static loading of 0.5 g (HV<sub>0.5</sub>) on both the cross-section of the specimen and the hot-rolling surface.

LT01 and LT02 represented two FCG specimens in the LT direction, while two others were in the TL direction, designated as TL01 and TL02. The notch crack length ( $a_n$ ), as shown in Fig. 1b, is 8.00 mm. The specimen was pre-fatigued under a constant load range ( $\Delta P_p$ ) = 5.520 kN at a stress level ( $R$ ) = 0.1 using true sinusoidal waves at a frequency ( $f$ ) of 10 Hz. The pre-fatigue loading was terminated once the total pre-crack length ( $a_p$ ) reached approximately 9.20 mm. Subsequently, the FCG test continued under a constant load range ( $\Delta P_{FCG}$ ) of 6.957 kN at  $R = 0.1$  and  $f = 10$  Hz until the specimen reached its failure point. To measure the crack mouth opening displacement (CMOD), a crack opening displacement (COD) gauge (Epsilon 3541-008M-040M-LT) with a gauge length of 8.00 mm was used. The crack length ( $a$ ) for the CT specimen was calculated using the compliance method [20], as outlined in Equation 1:

$$a = W(1.0010 - 4.6695U + 18.460U^2 - 236.82U^3 + 1214.9U^4 - 2143.6U^5) \quad (1)$$

Moreover, the value of  $U$  was calculated using Equation 2:

$$U = \frac{1}{[1+(ECB)^{1/2}]} \quad (2)$$

Where  $C$  is the  $v$ /load,  $v$  is the CMOD between measurement points,  $W$  and  $B$  are the specimen dimensions for the width of 40 mm and the thickness of 6 mm in Fig. 1b, respectively, and  $E$  is the elastic modulus. The crack length ( $a$ ) was calculated in increments of 2000 cycles. The number of cycles ( $N$ ) was plotted against the crack length ( $a$ ), and the Secant method [20] was used to calculate the crack growth rate ( $da/dN$ , mm/cycle) using Equation 3, which is expressed as follows:

$$(da/dN)_{\bar{a}} = (a_{i+1} - a_i)/(N_{i+1} - N_i) \quad (3)$$

The calculation of  $da/dN$  is based on an average rate over the  $(a_{i+1} - a_i)$  increment, and the average crack length,  $\bar{a} = \frac{1}{2}(a_{i+1} + a_i)$ , is used for the calculation of  $\Delta K$  using Equation 4 [20]:

$$\Delta K = \frac{\Delta P}{B\sqrt{W}} \frac{(2+\alpha)}{(1-\alpha)^{3/2}} (0.886 + 4.6\alpha - 13.32\alpha^2 + 14.72\alpha^3 - 5.6\alpha^4) \quad (4)$$

Where  $\alpha = \bar{a}/W$ , the  $da/dN$  and  $\Delta K$  pair data were plotted on double logarithmic  $x$ - $y$  axes. The FCG properties, including the constants  $C$  and  $m$  in the stable crack growth stage, were determined using the linear regression fitting technique.

### 2.3 Microstructural and Fracture Observation

The resin mounting of specimens and the subsequent steps of grinding and polishing were carried out sequentially to achieve a smooth, mirror-like surface on the specimen. The steel surface was then etched with 3% Nital for a few seconds, and the microstructures of SUP9 steel were observed using an optical microscope (Olympus B51X series) on both the cross-sectional side and the surface side along the rolling direction.

Fractographic images of the FCG specimens were taken using Field Emission-Scanning Electron Microscopy (Thermo-Fisher Scientific Quattro FE-SEM) in the fatigue crack growth zone at crack lengths of approximately 3 mm (stable crack growth) and 9 mm (rapid crack growth) from the pre-crack point,  $a_p = 9.2$  mm. EDS characterisations were conducted to analyse the elemental composition of the fractured specimen at specific points and across the entire surface area (in mass %).

## 3. RESULTS AND DISCUSSION

### 3.1 Microstructural Observation

The typical SUP9 steel microstructures on the cross-sectional and surface sides are presented in Figs. 2a and 2b, respectively. The optical microscope observations in Fig. 2 confirm the presence of predominantly pearlitic microstructures, with a minor component of ferrite. Significant differences in the steel's microstructure are evident across the ferrite grain sizes. The ferrite grain in Fig. 2a exhibits a smaller, elongated shape, whereas the ferrite grain in Fig. 2b shows a larger, rounded shape. Similar microstructures were observed in 42Cr4Mo steel resulting from the hot forging process [22], where pearlite and ferrite grain structures, formed during multidirectional hot forging [23,24], play a significant role in enhancing the mechanical properties of high-strength, low-alloy steel [22-24].

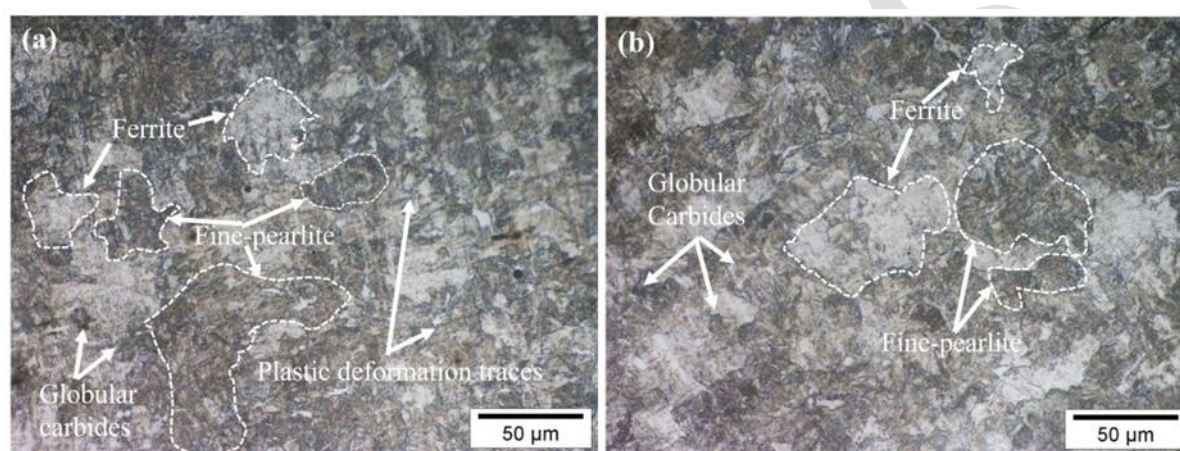


Fig. 2. Typical microstructures of SUP9 steel under hot-rolling conditions observed on (a) the cross-sectional side and (b) the longitudinal surface

The plastic deformation resulting from dislocation locking during the hot-rolling process led to a reduction in the interlamellar spacing of cementite ( $Fe_3C$ ) in the pearlite (Fig. 2a). Interlamellar spacing in pearlite refers to the distance between adjacent lamellar  $Fe_3C$  and ferrite matrix within the pearlite microstructure. Consequently, the phase boundary area among the lamellae of  $Fe_3C$  in the ferrite matrix was markedly reduced, which is believed to contribute to the formation of fine-pearlitic structures in the microstructure of SUP9 steel. As demonstrated in Fig. 2a, traces of plastic deformation can be observed in the region between the pearlite grain and the ferrite grain. Moreover, lamellae of  $Fe_3C$  precipitated in a ferrite matrix have been shown to play a crucial role in enhancing the tensile strength of SUP9 steel under hot-rolling conditions, as shown in Fig. 3. The interlamellar spacing is slightly larger on the cross-sectional side, suggesting that the microstructure may be

influenced by recrystallisation and growth occurring during the rolling process [17]. Consequently, the hardness level on the cross-sectional side ( $338.0 \pm 6$  HV) is higher than on the surface side ( $309.7 \pm 4.0$  HV).

### 3.2 Mechanical Properties of SUP9 Steel

Fig. 3 presents the typical engineering stress-strain curve of SUP9 steel in the hot-rolling condition. Additionally, an average value with a standard deviation, determined from two specimens, is displayed in Table 1, confirming that hot-rolled SUP9 steel exhibits the material's high mechanical strength. The engineering stress-strain curve (the green short-dot cycles in Fig. 3) shows minimal yielding behaviour, which occurred up to a strain of 0.0043 mm/mm. This characteristic can be attributed to the formation of microplasticity in the Lüders band zone [25,26] resulting from a small amount of obstacle dislocation movement. This observation is supported by microstructural analysis: a decrease in ferrite grain size and traces of plastic deformation in Fig. 2a. Therefore, the yield point, appearing at the beginning of tensile deformation, was determined from the intersection point between the 0.2% offset line and the stress-strain curve (Fig. 3). One intriguing observation is the high ratio of yield strength to ultimate strength, reaching 0.623, in SUP9 steel, which exhibits microplasticity-induced behaviour similar to the Lüders behaviour observed in X80 pipe steel [27].

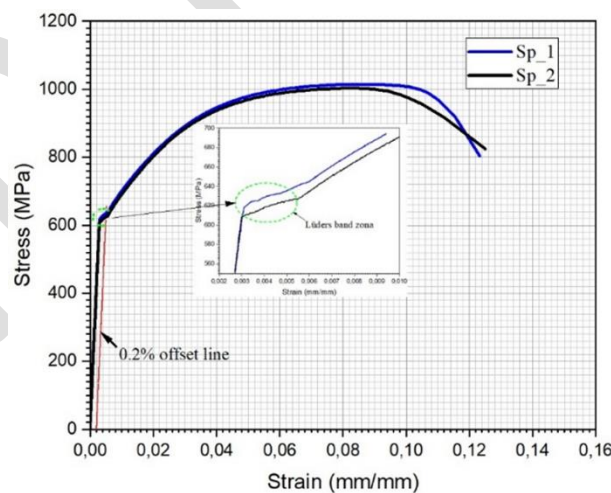


Fig. 3. Stress-strain curve of SUP9 steel in the hot-rolling condition

Table 1. Tensile properties of SUP9 steel under hot-rolling condition

Tensile strength (MPa)		$E$ (GPa)	Elongation, $e$ (%)	Strain hardening constant	
$\sigma_{\text{yield}}$	$\sigma_{\text{ult}}$			$K$ (MPa)	$n$
$630.63 \pm 7.88$	$1008.29 \pm 8.30$	$206.99 \pm 2.15$	$12.414 \pm 0.13$	$2014.05 \pm 3.86$	$0.244 \pm 0.02$

It is well known that the volume fraction of each phase (eutectoid ferrite and pearlite) within the microstructure is the primary determinant of the tensile properties and hardness of pearlitic ferrite steel [18], with the strength of pearlite following the Hall-Petch relationship with lamellar distance [28,29]. Furthermore, the steel gradually underwent high plastic deformation until a strain of 0.065 mm/mm. Later, the dislocation movements ceased, indicating that plastic deformation reached a maximum at a total strain of 0.076 mm/mm. Subsequently, the steel exhibited softening behaviour. The reduction of area at the higher point of stress concentration indicates dislocation annihilation.

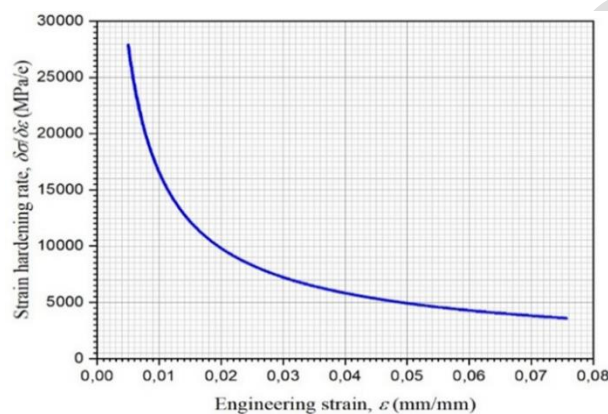


Fig. 4. The relationship between strain hardening rate and engineering strain

The limitation of SUP9 steel in terms of enabling deformation can be investigated by constructing the strain-hardening rate versus the engineering strain curve (Fig. 4). Fig. 4 shows that the steel has the greatest strain-hardening capability at a strain of 0.0050 mm/mm, with a gradual decrease in the strain-hardening rate indicated by an increase in strain up to 0.065 mm/mm. A similar investigation of hot-rolled low-carbon steel (SM490) found that fine pearlite resulted in high-angle grain boundaries (HAGB) in the longitudinal direction and low-angle boundaries (LAB) in the transverse direction [30]. Therefore, it is concluded that the co-existence of both low and high-angle boundaries formed due to axial deformation contributes to a significant increase in tensile strength over the uniform strain range. Fig. 4 justifies that the axial deformation induced in the steel at a ranging strain between 0.005 and 0.065 mm/mm via the interaction of dislocation movements contributed to work hardening [31]. In line with the dislocation density in high-strength low-alloy steel (42CrMo steel), Huang et al. [22] reported that the density of dislocations in 42CrMo steel increased by 3.81 times due to plastic deformation compared with the initial dislocation density before hot-forging. Furthermore,



dislocations move continuously in the phase boundary area consisting of lamellar  $\text{Fe}_3\text{C}$  until a uniform strain of approximately 0.076 mm/mm (Fig. 4). Rapid dislocation annihilations are indicated by the reduction in the localisation area of the tensile specimen, a phenomenon known as necking.

### 3.3 Fatigue Crack Growth Behaviour

Fig. 5 shows the relationship between crack length ( $a$ ) and the number of cycles ( $N$ ) obtained from FCG tests for LT and TL specimens. Compared to cracks propagating in the LT specimens, those propagating in the TL specimens exhibit the most extended fatigue cycles to failure. The lamellae of  $\text{Fe}_3\text{C}$  in the pearlite phase (Fig. 2a) play a crucial role in retarding crack propagation. This is achieved through the crack closure mechanism at the crack tip, which enhances the material's stability and resilience. Accordingly, the total number of fracture cycles for SUP9 steel in the LT direction is approximately 54,000 cycles, which is 6,099 cycles lower than that of SUP9 steel in the TL direction.

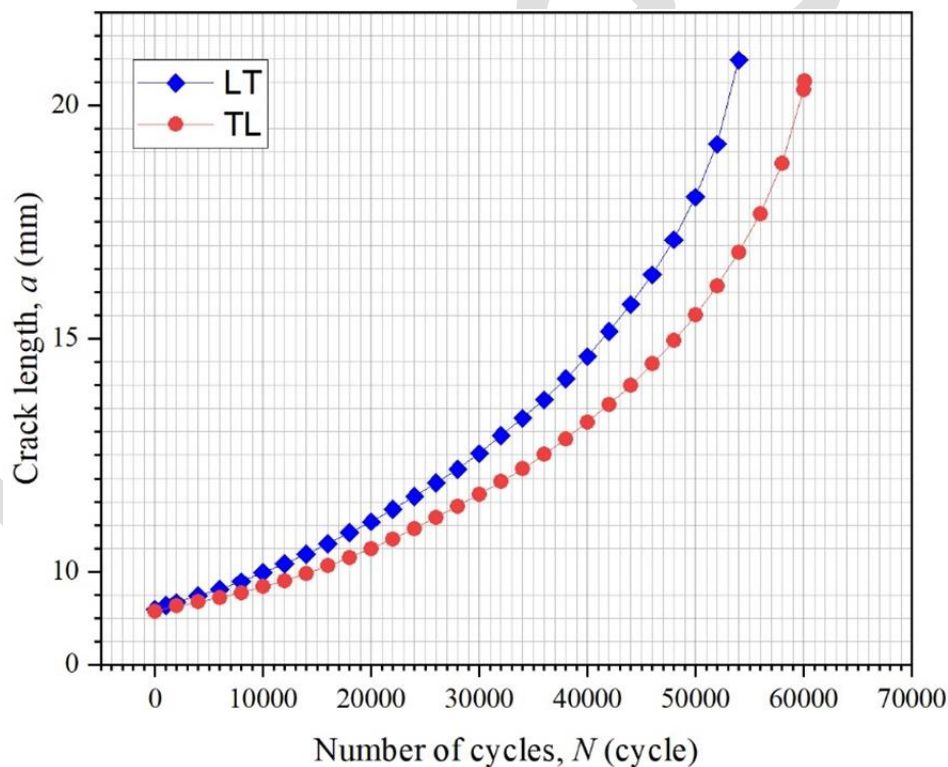


Fig. 5. Fatigue crack length as a function of the number of cycles for SUP9 steel in different crack plane orientations

Significant differences in crack propagation between LT and TL specimens emerge once the cracks propagate over 5,000 cycles. The crack in the TL specimen is consistently more prolonged than that in the LT specimen for the same number of cycles. A similar FCG behaviour has been observed in the

ferrite-pearlite microstructure of hot-rolled low-alloy steel [13,15]. The substantial plastic deformation experienced by SUP9 steel in the longitudinal direction leads to much more effective retardation of crack propagation. This finding confirms that fractures in leaf spring steel result from crack propagation in the transverse direction [2-4,8,32,33].

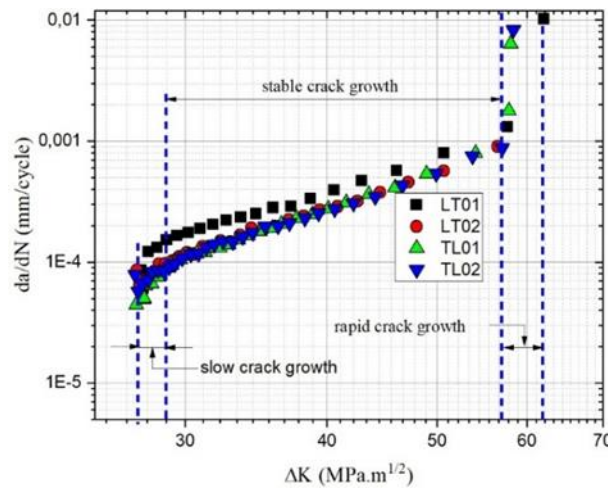


Fig. 6. Relationship between  $\Delta K$  and  $da/dN$

Fatigue crack growth (FCG) behaviour can be investigated in three zones [34]: (1) the slow crack growth zone, (2) the stable crack growth zone, and (3) the rapid crack growth zone. However, the most valuable insights into fatigue crack growth behaviour are typically gained in the stable crack growth zone. This is achieved by determining the fatigue crack growth rate ( $da/dN$ ) corresponding to the stress intensity factor range ( $\Delta K$ ). The fatigue crack growth rate ( $da/dN$ ) and the stress intensity factor range ( $\Delta K$ ) for LT and TL specimens are plotted in Fig. 6 on a double logarithmic  $x$ - $y$  axes scale.

Based on the Paris-Erdogan law, empirically expressed in Equation 5, it can be concluded that in the linear part of the stable crack growth stage, there are significant differences in the FCG behaviour of LT and TL specimens

$$\frac{da}{dN} = C(\Delta K)^m \quad (5)$$

Where:

$C$  = an experimentally determined constant

$m$  = the exponent for the crack growth rate

Additionally, Figs. 7(a-d) show the corresponding  $da/dN$  vs.  $\Delta K$  curves for each specimen in the LT and TL directions. In Fig. 7, the calculated  $C$  and  $m$  values from Equation 5 are obtained using the

linear fitting regression method, representing the FCG properties. The average  $C$  and  $m$  values derived from the two CT specimens in the LT and TL directions are presented in Table 2.

The lower constant value of  $m$  obtained from the TL specimens indicates that cracks propagating in the longitudinal direction expand more slowly than those in the transverse direction. A similar behaviour was observed in 51CrV4 spring steel under QT conditions, where cracks propagated faster in the transverse than in the longitudinal direction [33].

The hot-rolling process has been demonstrated to markedly reduce the interlamellar spacing [31]. This refers to the distances between the lamellar  $\text{Fe}_3\text{C}$  in the pearlite phase across the material's thickness in the longitudinal direction. Consequently, the crack tip driving force is effectively reduced through mechanisms such as crack tip blunting and deflection [34]. The value of  $m$  for SUP9 steel under hot-rolling conditions is lower than the  $m$  value (3.64) for AISI 4140 under annealing conditions [35].

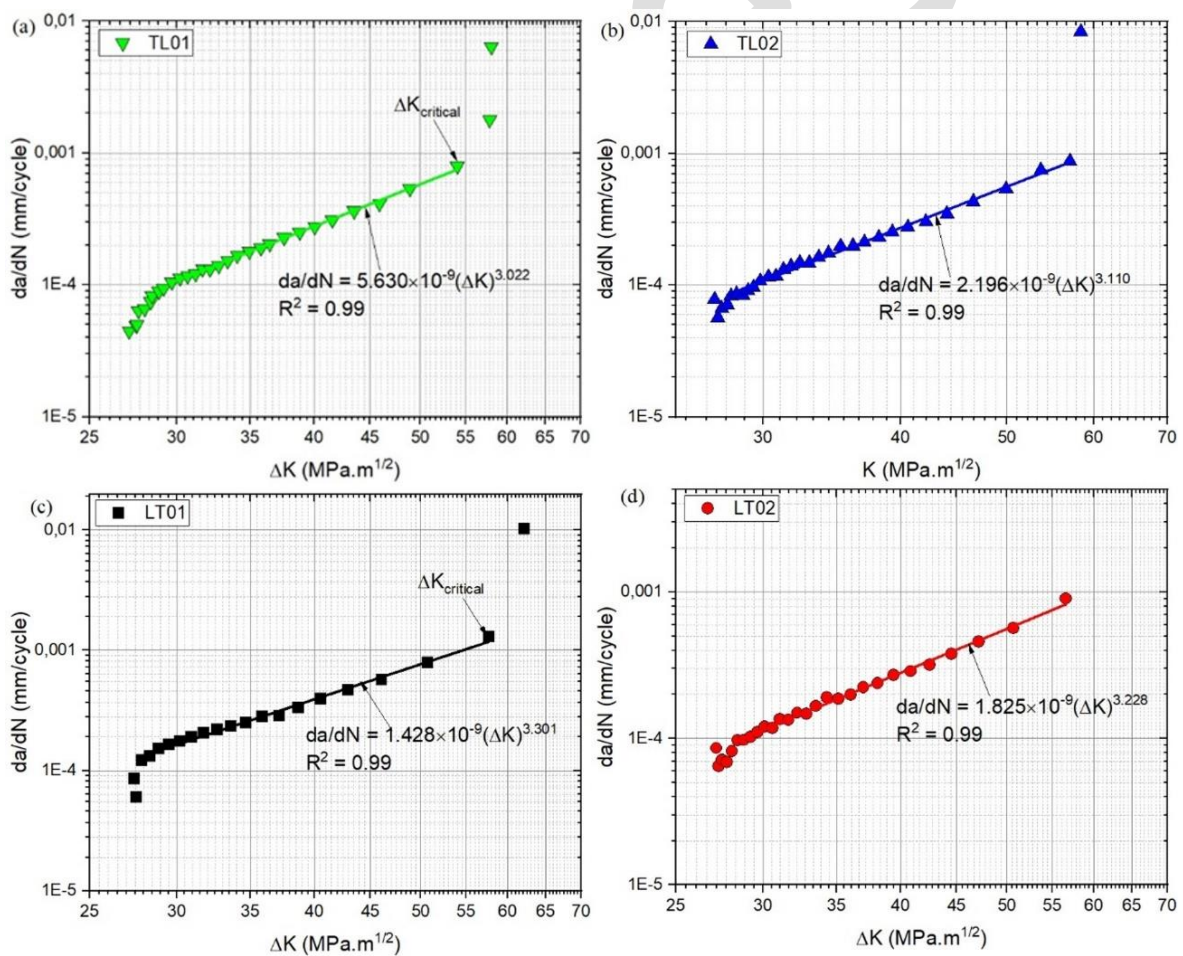


Fig. 7. Plot of  $\Delta K$  versus  $da/dN$  obtained from the present research for (a-b) TL and (c-d) LT specimens, along with calibration curves using the linear curve-fitting regression method

Furthermore, the high dislocation density and deformation potential in specimens oriented in the TL direction leads to a more significant retardation of fatigue crack growth compared to specimens oriented in the LT direction. A reduction in interlamellar spacings between the ferrite matrix and the lamellar Fe<sub>3</sub>C decreases the frequency of cracks encountering pearlite. Consequently, the crack path becomes more tortuous, thereby slowing the crack propagation rate. The range of  $\Delta K$  for SUP9 steel, observed in Fig. 6 during stable crack growth, is approximately 27.84–57.69 MPa.m<sup>1/2</sup>. This range is slightly higher than that observed in ferrite-pearlite low-carbon steel (15.4–51.4 MPa.m<sup>1/2</sup>) [34] under the same hot-rolling conditions. Similarly, 51CrV4 leaf spring steel in QT conditions displays reduced maximum  $\Delta K$  values [33] in comparison to SUP9 leaf spring steel under hot-rolling conditions, which has a critical crack point of approximately 20 mm.

Table 2. FCG properties of SUP9 steel

Crack plane orientation	Fatigue crack growth rate constants	
	$C$ (mm/cycle)	$m$
TL	$(3.913 \pm 2.428) \times 10^{-9}$	$3.066 \pm 0.062$
LT	$(1.627 \pm 0.281) \times 10^{-9}$	$3.265 \pm 0.052$

### 3.4 Fractographical Observation

The SEM images in Fig. 8 display the fracture surface morphologies of the LT and TL specimens in the different fatigue crack growth zones. The SEM images in Figs. 8a and 8c indicate that the stable crack zones ( $\Delta K = 32.62$  MPa.m<sup>1/2</sup>) exhibit striation fatigue cracks spread throughout the surface fracture of the pearlite region, appearing as distinct parallel lines or ridges perpendicular to the direction of crack propagation. These striations result from cyclic loading and represent incremental crack growth during each loading cycle. Numerous cleavage surface cracks are observed in the ferrite region, as the ferrite's lower plastic deformation capacity makes it more susceptible to cleavage [14]. At the phase boundary in the pearlite region, irregular small cracks were observed. Additionally, secondary cracks appeared on the fatigue fracture surfaces at the pearlite-ferrite phase boundary, as shown in Fig. 8.

Secondary cracks and branching may be visible alongside the primary fatigue crack on the fracture surface. The secondary crack initially formed due to intergranular propagation along the grain boundary between the weak ferritic and hard pearlitic phases [15]. These secondary features result from interactions between the primary crack and the material microstructure, such as grain boundaries



or inclusions. Consequently, secondary cracks can influence the material's overall fatigue behaviour and failure mode in the rapid crack zone, where  $\Delta K$  is approximately  $46.07 \text{ MPa}\cdot\text{m}^{1/2}$ . The secondary crack observed in Figs. 8c and 8d becomes more extensive and longer as the number of fatigue cycles increases. As mentioned above, the pearlite structure in the longitudinal direction is tougher than that in the transverse direction. Consequently, the crack propagating in the longitudinal direction becomes blunted and slightly curved, leading to crack arrest (Fig. 8b).

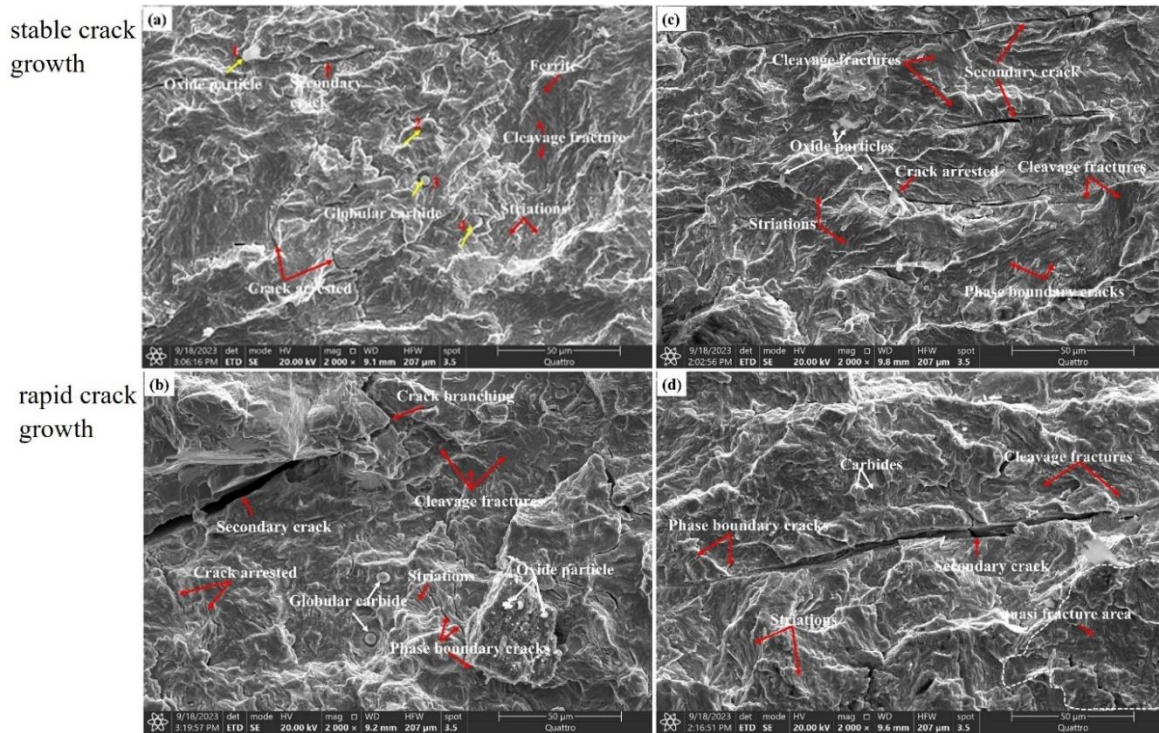


Fig. 8. SEM fracture morphologies of (a-b) TL and (c-d) LT specimens at different FCG zones

Some non-metallic inclusions containing oxide particles and manganese sulphides (MnS) were found to significantly influence the FCG behaviour of low-alloy steels, as reported in previous studies [34,36,37]. The SEM observations shown in Fig. 8 confirm the formation of inclusions in the microstructures of the SUP9 steel produced by the hot-rolling process. The SEM surface morphology combined with EDS point analysis in Fig. 8a confirms that the spherical oxide particle contains elements in the following proportions: 54.08C, 6.25Si, 21.84O, 14.99Ni, 2.83Al, 0.81Na, 0.60S, 0.50Ca, and 7.19Fe (denoted by the yellow arrow and point 1). The dark, smaller regions, indicated by the yellow arrow as well as points 2 and 4, contain elements of 31.22C-0.53Mn-68.26Fe and 36.22C-

0.58Mn-63.20Fe, respectively. Meanwhile, the spherical carbide (point 3) contains 22.80C-0.94Si-1.38Mn-5.52S-10.34Fe (Fig. 8b).

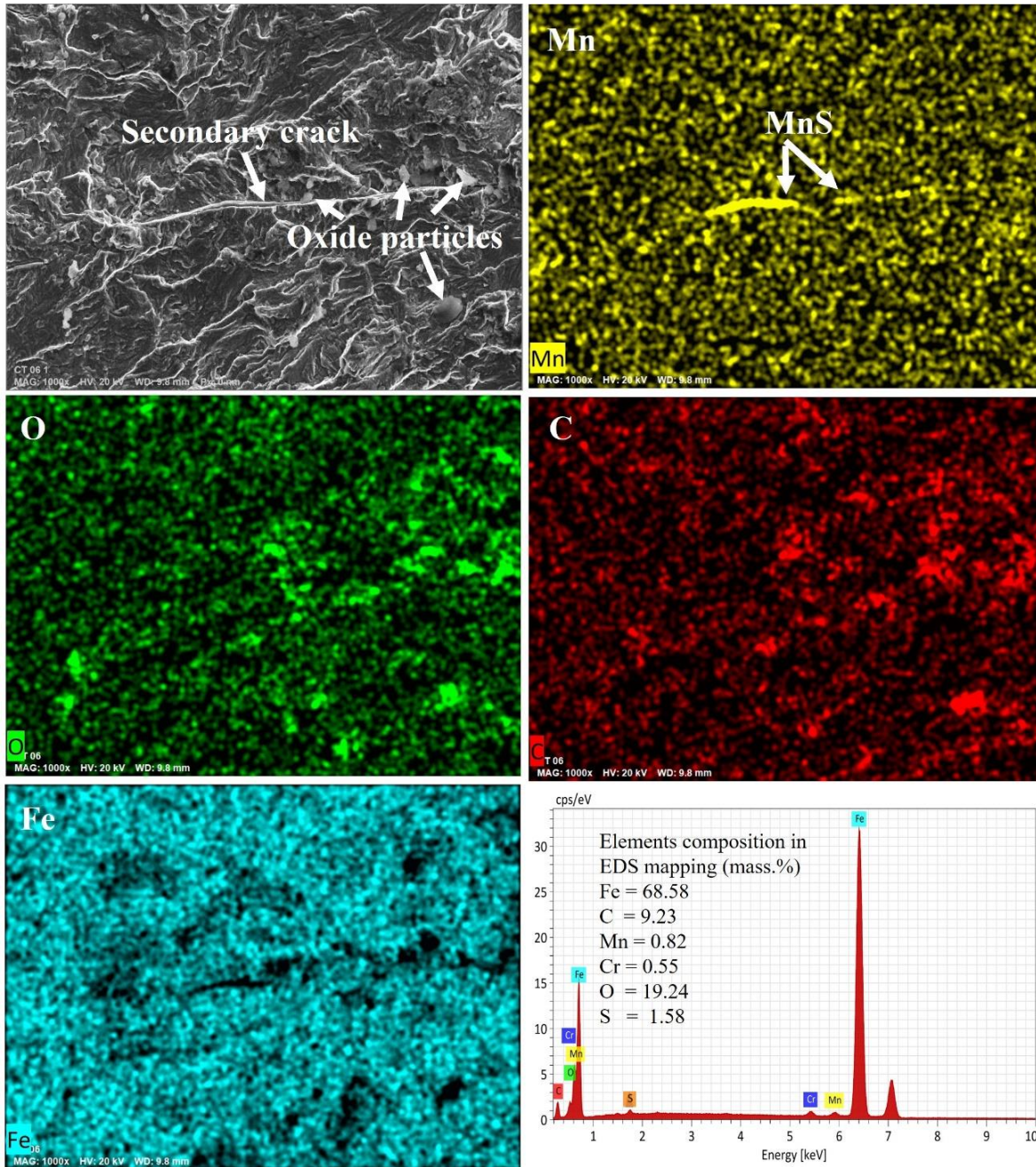


Fig. 9. SEM fractographic surface of the LT specimen observed at a crack length of approximately 0.3 mm, showing the elemental mapping of Mn, O, C, Fe, and the corresponding EDS spectra

Fig. 9 illustrates the elongated shape of the manganese sulphide (MnS) embedded within the secondary crack. As confirmed by EDS elemental mapping and spectral analysis (Fig. 9), some inclusions contain oxides. Our research suggests that the presence of oxide particles and MnS in the



steel microstructure can influence the steel's fatigue crack growth behaviour. The effect of these inclusions depends, among other factors, on their size, composition, content, and distribution [36]. However, the elongated MnS inclusion has less impact on fatigue crack propagation than oxide inclusion due to the higher stress localisation caused by the oxide [36,38]. MnS precipitation at the grain boundary was observed in the LT specimen (Fig. 9), resulting in accelerated intergranular cracking [39]. At a critical crack length of 20 mm, MnS precipitation in the secondary crack causes rapid crack propagation (Fig. 8d), leading to complete fracture.

## CONCLUSIONS

Following an investigation into the mechanical strength and fatigue crack growth behaviour of hot-rolled SUP9 steel, it has been determined that this material is suitable for use in leaf spring suspension applications. The following conclusions can be drawn from the investigation:

1. The small phase boundary between lamellar  $\text{Fe}_3\text{C}$  in pearlitic structures and elongated ferrite grains in the microstructure of hot-rolled SUP9 steel, examined in the longitudinal direction, is instrumental in enhancing mechanical strength. The material exhibits high tensile strength, favourable hardness, and a microstructure that balances strength with resistance to fatigue crack growth.
2. SUP9 steel demonstrates enhanced resistance to fatigue crack growth in the longitudinal direction. Conversely, cracks propagating in the transverse direction significantly accelerate crack expansion. This behaviour is influenced by various factors, including intergranular cracks caused by MnS precipitates, ductile fracture at lamellar carbide boundaries, and cleavage fracture within the ferrite phase.
3. The SEM fractural surface analysis indicates the presence of spherical oxide precipitation, irregular carbide shapes, and the splitting of phase boundaries. These features are observed in the cracking area during the crack growth stages, where evidence of fatigue is visible and secondary cracks are present. The morphology of the crack propagation area shows striations in the pearlite regions.

## DATA AVAILABILITY

All experimental data requested are available upon request from the corresponding author.

## ACKNOWLEDGEMENT

We gratefully acknowledge the financial support of Universitas Lampung through the Magister Research Grant, contract number 552/UN26.21/PN/2024.

## REFERENCES

- [1] Kong, Y. S., Abdullah, S., Omar, M. Z. and Haris, S. M., "Failure assessment of a leaf spring eye design under various load cases". *Eng. Fail. Anal.*, 2016, 63, 146-159. <https://doi.org/10.1016/j.engfailanal.2016.02.017>.
- [2] James, M. N., Hattingh, D. G. and Matthews, L., "Embrittlement failure of 51CrV4 leaf springs". *Eng. Fail. Anal.*, 2022, 139, 106517. <https://doi.org/10.1016/j.engfailanal.2022.106517>.
- [3] Daudpoto, J., Kumar, D., Shaikh, S. A., Hussain, T. and Memon, Z. A., "Fatigue failure of SUP-9 spring steel". *Maters. Res. Express*, 2021, 8(6), 066509. <https://doi.org/10.1088/2053-1591/ac0773>.
- [4] Infante, V., Freitas, M. and Baptista, R., "Failure analysis of a parabolic spring belonging to a railway wagon". *Eng. Fail. Anal.*, 2022, 140, 106526. <https://doi.org/10.1016/j.engfailanal.2022.106526>.
- [5] Kumar, S. R., Sreeravind, M., Sainathan, S., Venkat, A., Rahulram, S., Kumar, S. S. and Kumaran, S. S., "Low cycle fatigue behavior of heat treated EN-47 spring steel". *Materials Today: Proceedings*, 2020, 22, 2191-2198. <https://doi.org/10.1016/j.matpr.2020.03.299>.
- [6] Kubit, A., Bucior, M., Zielecki, W. and Stachowicz, F., "The impact of heat treatment and shot peening on the fatigue strength of 51CrV4 steel". *Proc. Struc. Integ.*, 2016, 2, 3330-3336. DOI: <https://doi.org/10.1016/j.prostr.2016.06.415>.
- [7] Scuracchio, B. G., de Lima, N. B. and Schön, C. G., "Role of residual stresses induced by double peening on fatigue durability of automotive leaf springs". *Mater. Des.*, 2013, 47, 672-676. <https://doi.org/10.1016/j.matdes.2012.12.066>.
- [8] Cheng, G., Chen, K., Zhang, Y. and Chen, Y., "The fracture of two-layer leaf spring: Experiments and simulation". *Eng. Fail. Anal.*, 2022, 133, 105971. <https://doi.org/10.1016/j.engfailanal.2021.105971>.
- [9] Ganesh, P., Sundar, R., Kumar, H., Kaul, R., Ranganathan, K., Hedao, P., Raghavendra, G., Anand, K. S., Tiwari, P. and Nagpure, D. C., "Studies on fatigue life enhancement of pre-fatigued spring steel specimens using laser shock peening". *Maters. Des.*, 2014, 54, 734-741. <https://doi.org/10.1016/j.matdes.2013.08.104>.
- [10] Podgornik, B., Leskovšek, V., Godec, M. and Senčič, B., "Microstructure refinement and its effect on properties of spring steel". *Maters. Sci. Eng. A*, 2014, 599, 81-86. <https://doi.org/10.1016/j.msea.2014.01.054>.
- [11] Zhou, C., Chi, M., Wen, Z., Wu, X., Cai, W., Dai, L., Zhang, H., Qiu, W., He, X. and Li, M., "An investigation of abnormal vibration-induced coil spring failure in metro vehicles". *Eng. Fail. Anal.*, 2020, 108, 104238. <https://doi.org/10.1016/j.engfailanal.2019.104238>.
- [12] Królicka, A., Lesiuk, G., Radwański, K., Kuziak, R., Janik, A., Mech, R. and Zygmunt, T., "Comparison of fatigue crack growth rate: Pearlitic rail versus bainitic rail". *Intl. J. Fat.*, 2021, 149, 106280. <https://doi.org/10.1016/j.ijfatigue.2021.106280>.
- [13] Ogawa, Y., Nishida, H., Nakamura, M., Olden, V., Vinogradov, A. and Matsunaga, H., "Dual roles of pearlite microstructure to interfere/facilitate gaseous hydrogen-assisted fatigue crack growth in plain carbon steels". *Intl. J. Fat.*, 2022, 154, 106561. <https://doi.org/10.1016/j.ijfatigue.2021.106561>.
- [14] Badaruddin, M., Sugiyanto, Wardono, H., Andoko, Wang, C. J. and Rivai, A. K., "Improvement of low-cycle fatigue resistance in AISI 4140 steel by annealing treatment". *Intl. J. Fat.*, 2019, 125, 406-417. <https://doi.org/10.1016/j.ijfatigue.2019.04.020>.
- [15] Igwemezie, V., Dirisu, P. and Mehmanparast, A., "Critical assessment of the fatigue crack growth rate sensitivity to material microstructure in ferrite-pearlite steels in air and marine



- environment*". *Maters. Sci. Eng. A*, 2019, 754, 750-765.  
<https://doi.org/10.1016/j.msea.2019.03.093>.
- [16] Qian, C., Shi, W., Chen, Z., Yang, S., and Song, Q., "Fatigue reliability design of composite leaf springs based on ply scheme optimisation". *Compos. Struct.* 2017, 168, 40-46.  
<https://doi.org/10.1016/j.compstruct.2017.02.035>.
- [17] Maya, J. S., Ramirez, A. J. and Toro, A., "Fatigue crack growth rate of two pearlitic rail steels". *Eng. Frac. Mech.* 2015, 138, 63-72. <https://doi.org/10.1016/j.engfracmech.2015.03.023>.
- [18] Zeng, D., Wang, J., Lu, L., Shen, C., Guo, J., Xu, T. and Wang, Z., "Fatigue crack growth behavior of railway wheel steel modified by sulfides enveloping oxides inclusions". *Intl. J. Fat.*, 2023, 175, 107811. <https://doi.org/10.1016/j.ijfatigue.2023.107811>.
- [19] ASTM E8, Standard Test Methods for Tension Testing of Metallic Materials. 2004, ASTM International, West Conshohocken, PA, United States.
- [20] ASTM E647, Standard Test Method for Measurement of Fatigue Crack Growth Rates. 2000, ASTM International, West Conshohocken, PA, United States.
- [21] ASTM E646, Standard Test Method for Tensile Strain-Hardening Exponents (n -Values) of Metallic Sheet Materials. 2000, ASTM International, West Conshohocken, PA, United States..
- [22] Huang, W., Zhong, H., Lei, L. and Fang, G., "Microstructure and mechanical properties of multi-pass forged and annealed 42CrMo steel". *Maters. Sci. Eng. A*, 2022, 831, 142191.  
<https://doi.org/10.1016/j.msea.2021.142191>.
- [23] Zhang, L., Yang, W., Cheng, Q., Wang, H., Zheng, S., Li, M., Duan, Y., Xu, Z. and Xi, Y., "The effect of different forging ratios on the properties and microstructures of high strength steel 40CrNi2Si2MoV". *J. Mater. Res. Technol.*, 2024, 29, 2326-2338.  
<https://doi.org/10.1016/j.jmrt.2024.01.277>.
- [24] Song, G., Ji, H., Pei, W., Li, J., Zhao, J., Xiao, W. and Wang, B., "Prediction of microstructure evolution during multidirectional forging of the railway wagon bogie adpter". *Maters. Today Comm.* 2022, 32, 104143. <https://doi.org/10.1016/j.mtcomm.2022.104143>.
- [25] Tsuchida, N., Tomota, Y., Nagai, K. and Fukaura, K., "A simple relationship between Lüders elongation and work-hardening rate at lower yield stress". *Scrip. Materia.* 2006, 54(1), 57-60.  
<https://doi.org/10.1016/j.scriptamat.2005.09.011>.
- [26] Zhang, Y., Shuai, J., Lv, Z., Ren, W. and Zhang, T., "Effect of the Lüders plateau on the relationship between fracture toughness and constraint for pipeline steels". *Theor. Appl. Fract. Mech.*, 2022, 119, 103354. <https://doi.org/10.1016/j.tafmec.2022.103354>.
- [27] Han, J., Lu, C., Wu, B., Li, J., Li, H., Lu, Y. and Gao, Q., "Innovative analysis of Luders band behaviour in X80 pipeline steel". *Maters. Sci. Eng. A*, 2017, 683, 123-128.  
<https://doi.org/10.1016/j.msea.2016.12.008>.
- [28] Mishra, K. and Singh, A., "Effect of interlamellar spacing on fracture toughness of nano-structured pearlite". *Maters. Sci. Eng. A*, 2017, 706, 22-26.  
<https://doi.org/10.1016/j.msea.2017.08.115>.
- [29] Steffen, S., Bernhard, A. and Javad M., "Impact of interlamellar spacing and non-pearlitic features on mechanical properties and cyclic damage initiation in near-eutectoid pearlitic steels". *Maters. Sci. Eng. A*, 2024, 889, 145846. <https://doi.org/10.1016/j.msea.2023.145846>.
- [30] Liu, B. X., Fan, K. Y., Yin, F. X., Feng, J. H. and Ji, P. G., "Effect of caliber rolling reduction ratios on the microstructure and mechanical properties of 45 medium carbon steel". *Maters. Sci. Eng. A*, 2020, 774, 138954. <https://doi.org/10.1016/j.msea.2020.138954>.
- [31] Song, Z. H., Song, H. Y., Liu, J. X. and Liu, H. T., "Tuning heterogeneous microstructure and improving mechanical properties of twin-roll strip cast low carbon steels by on-line heat treatments". *J. Mater. Res. Technol.*, 2024, 30, 5894-5904.  
<https://doi.org/10.1016/j.jmrt.2024.04.143>.
- [32] Kong, Y. S., Omar, M. Z., Chua, L. B. and Abdullah, S., "Fatigue life prediction of parabolic leaf spring under various road conditions". *Eng. Fail. Anal.*, 2014, 46, 92-103.  
<https://doi.org/10.1016/j.engfailanal.2014.07.020>.
- [33] Gomes, V. M. G., Lesiuk, G., Correia, J. A. F. O. and de Jesus, A. M. P., "Fatigue crack propagation of 51CrV4 steels for leaf spring suspensions of railway freight wagons". *Materials*, 2024, 17(8), 1831. <https://doi.org/10.3390/ma17081831>.

- [34] Li, S., Kang, Y. and Kuang, S., "Effects of microstructure on fatigue crack growth behavior in cold-rolled dual phase steels". *Maters. Sci. Eng. A*, 2014, 612, 153-161. <https://doi.org/10.1016/j.msea.2014.06.002>.
- [35] Badaruddin, M., Sugiyanto, Sumardi, S. and Asmi, D., "Improvement of the fatigue crack growth resistance in AISI 4140 steel under single- and multi-austempering heat treatments". *Res. in Eng.* 2024, 21, 101814. <https://doi.org/10.1016/j.rineng.2024.101814>.
- [36] Li, Z. D., Zhou, S. T., Yang, C. F. and Yong, Q. I., "High/very high cycle fatigue behaviors of medium carbon pearlitic wheel steels and the effects of microstructure and non-metallic inclusions". *Maters. Sci. Eng. A*, 2019, 764, 138208. <https://doi.org/10.1016/j.msea.2019.138208>.
- [37] Furuya, Y., "Gigacycle fatigue of high-strength steel caused by MnS inclusions". *Maters. Sci. Eng. A*, 2021, 824, 141840. <https://doi.org/10.1016/j.msea.2021.141840>.
- [38] Heshmati, N., Athar, M. H., Borgenstam, A., Sieurin, H., Larsson, J. and Hedström, P., "Microstructural influences on simultaneous strength and fatigue crack resistance in advanced high-strength steels". *Intl. J. Fat.*, 2024, 184, 108278. <https://doi.org/10.1016/j.ijfatigue.2024.108278>.
- [39] Shi, W., Yang, S., Dong, A. and Li, J., "Understanding the corrosion mechanism of spring steel induced by MnS inclusions with different sizes". *JOM*, 2018, 70, 2513-2522. <https://doi.org/10.1007/s11837-018-3026-6>.

Im Press